LASER DIAGNOSTICS AND DNS OF TURBULENT PREMIXED FLAMES

Toshio Miyauchi, Mamoru Tanahashi, Masayasu Shimura,
Shohei Taka, Shingo Matsuura
Department of Mechanical and Aerospace Engineering,
Tokyo Institute of Technology
2-12-1 Ookayama, Meguro-ku, Tokyo 152-8550, Japan
tmiyauch@mes.titech.ac.jp, mtanahas@mes.titech.ac.jp, mshimura@navier.mes.titech.ac.jp,
shtaka@navier.mes.titech.ac.jp, matsuura@navier.mes.titech.ac.jp

ABSTRACT

With the developments of computer technologies, three-dimensional direct numerical simulations (DNS) of turbulent combustion have been realized with a detailed or reduced kinetic mechanism. The 3D DNS gives detailed information about turbulent flames, while there are few experimental techniques which have high accuracy enough to compare with DNS. In this paper, after showing summary of recent DNS of turbulent premixed flames, newly-developed laser diagnostics are presented. Simultaneous CH-OH planar laser induced fluorescence (PLIF) and stereoscopic particle image velocimetry (PIV) are used to investigate the local flame structure of the turbulent premixed flames. From CH-OH PLIF and PIV measurements, flame fronts are identified, and the curvature of the flame front and the tangential strain rate at the flame front are evaluated. The experimental results are compared with 3D DNS of hydrogen-air and methane-air turbulent premixed flames. The flame displacement speeds in turbulent premixed flames have been measured directly by the CH double-pulsed PLIF. Since the time interval of the successive CH PLIF can be selected arbitrarily, both of the large scale dynamics and local displacement of the flame front can be obtained. As an application of laser diagnostics for development of high-efficient and low-emission combustors, reconstruction of 3D flame structure is shown by using multiple-plane OH PLIF.

INTRODUCTION

Turbulent combustion is one of the most difficult problems in computational science, because this phenomenon includes very complicated interaction of turbulence and chemical reactions. In combustion chemistry, very fast elementary reactions need quite small time and spatial resolutions, which is well-known as a stiffness problem. Direct numerical simulations (DNS) of turbulent flows have been used for turbulence research in last few decades, whereas the first 3D DNS of turbulent combustion with a detailed kinetic mechanism has been reported in 2000 (Tanahashi et al., 2000a). The combustion can be classified into premixed flames and non-premixed (diffusion) flames. The characteristics of the turbulent premixed flames have been classified by the ratio of the laminar burning velocity (S_L) to the turbulence intensity (u'_{rms}) and the ratio of the laminar flame thickness (δ_F) to the turbulence length scale (l), which is called as turbulent combustion diagram (Peters, 1999). In the turbulent combustion diagram, the flame structure split into four regimes; wrinkled flamelets, corrugated flamelets, thin reaction zones and broken reaction zones. In the wrinkled flamelets and the corrugated flamelets regimes, local flame structure is considered to be laminar flame with small curvature under strain field, whereas characteristics of the flame elements in the thin reaction zones and the broken reaction zones are supposed to be quite different from that of laminar flame. However, actual flame structure in turbulence has not been clarified yet (Tanahashi et al., 2002).

In the recent 3D DNS, characteristics of the turbulent premixed flames are investigated extensively (Tanahashi et al., 2000; 2002; Bell et al., 2002; Jenkins and Cant, 2002; Nada et al., 2004; Sreedhara and Lakshmisha, 2002) and local flame structures which differ from theoretical classifications have been clarified. 3D flame structures, which are caused by strong fine scale eddies in turbulence and described as the handgrip and spire structures (Nada et al., 2004), appear even in the corrugated flamelets regime of the combustion diagram, and enhance flame wrinkling and local heat release rate. The importance of these structures should be investigated by the experiments.

To investigate turbulent flame structures experimentally, planar laser induced fluorescence (PLIF) of molecules and radicals produced by chemical reactions (Dyer and Crosley, 1985; Hanson, 1986) such as OH (Smooke et al., 1992), CO (Seitzman et al., 1987), CH (Allen et al., 1986; Carter et al., 1998; Mansour et al., 1998) and CH_2O (Bockle et al., 2000) are commonly used. Since OH radicals show high concentration in the burned gas, OH PLIF is useful to distinguish the burned gas from the unburned mixture. Although the edges of OH radical distribution may correspond to the flame fronts for low Reynolds number turbulent flames, there is a possibility that flame fronts do not exist at the edge of OH radicals in high Reynolds number cases in which flame front is significantly distorted and multiply folded. On the other hand, CH PLIF has been used to investigate characteristics of the flame front in turbulence because CH radicals are produced at the flame front and have very narrow width enough to represent the reaction zones (Allen et al., 1986; Mansour et al., 1998). However, it is hard to distinguish the unburned gases from burned gases only from the CH PLIF. To overcome these defects in single radical PLIF, simultaneous OH and CH PLIF has been developed and applied for turbulent non-premixed flames (Donbar et al., 2000).

In addition to the PLIF measurement, particle image velocimetry (PIV) has been adopted to measure turbulence characteristics near the flame (Kalt et al., 1998; Sinibaldi et al., 2003). Recently, simultaneous CH, OH and velocity measurement has been reported in non-premixed flame (Kothnur et al., 2002). However, almost all studies were restricted to 2D and two-component (2C) PIV to measure the velocity field with PLIF. To obtain the detailed information about turbulent velocity field, 3C velocity measurement such as a stereoscopic PIV (Arroyo and Greated, 1991; Prasad, 2000) is desirable.

The description of dynamics of flame front has been one

of the most important subjects in the turbulent combustion research since flame dynamics is the basis of turbulent combustion models in the flamelet concept (Clavin, 1985; Law and Sung, 2000; Peters, 2000; Pope, 1988; Williams, 1985; 2000). In the concept of the flame stretch, increasing rate of the flame area is expressed by flame displacement speed, flame curvature and strain rate at the flame front (Candel and Poinsot, 1990; Pope, 1988). In previous studies (Poinsot et al., 1992; Sinibaldi et al., 2003), the curvature and strain rate effects have been investigated in the steady or unsteady laminar flames because the flame elements in turbulent flames are assumed to be laminar flame under weak stretch with small curvature.

To confirm the flame stretch concept experimentally, measurements of the flame displacement speed are necessary. In general, shadowgraph or laser tomography has been adopted to estimate flame displacement (Kido et al., 2002; Sinibaldi et al., 2003). However, in these techniques, flame propagation normal to the flame front is assumed. In turbulent flames, the flame elements do not always move into the flame normal direction due to strong convection effects of turbulence. In the numerical investigations by DNS (Baum et al., 1994; Echekki and Chen, 1996; Haworth and Poinsot, 1992; Tanahashi et al., 2000a; van Oijen et al., 2005), consumption speed and local heat release rate are commonly used to represent characteristics of flamelets instead of the flame displacement speed. In experiments, however, measurements of the local consumption speed or heat release rate are quite difficult even by CH PLIF due to severe calibration problem.

Although the conventional PLIF has been a very powerful tool to obtain instantaneous local flame structures, investigation of dynamics of flame structures in turbulence has been difficult due to the limitation of time resolution. The time resolution of conventional PLIF measurement is of the order of Hz, which is limited by experimental instruments. Recently, several time-resolved PLIF have been reported (Kaminski et al., 1999; Kychakoff et al., 1987; Seitzman et al., 1994; Watson et al., 2002).

In this paper, after showing summary of recent DNS of turbulent premixed flames, newly-developed laser diagnostics of turbulent combustion are presented.

TURBULENT PREMIXED FLAMES PROPAGATING IN HOMOGENEOUS TURBULENCE

DNS of Turbulent Premixed Flames

Details of DNS can be found in Tanahashi et al. (2000a; 2005a). Numerical parameters of DNS are listed in Table 1. In Table 1, ratios of the most expected diameter of the fine scale eddy (D) of turbulence to δ_F are presented. D is 8 times Kolmogorov length (η) (Tanahashi et al., 2001; 2004a). As for hydrogen-air turbulent premixed flames, a detailed kinetic mechanism which includes 12 species and 27 elementary reactions is used and all of the DNS were conducted for $\phi = 1.0$, 700K and 0.1MPa. For methane-air turbulent premixed flames, a reduced kinetic mechanism which consists of 23 chemical species and 19 step reactions is used (Tanahashi et al., 2005a). A methane-air mixture in unburned side is set to be $\phi = 1.0$ at 0.1MPa and 950K. In the turbulent combustion diagram proposed by Peters (1999), HR37HS, HR97HM and MR37HS are classified into the thin reaction zones. HR37LL is classified into the wrinkled flamelets and other cases are into the corrugated flamelets.

Table 1: Numerical parameters for DNS of turbulent premixed flames propagating in homogeneous turbulence.

	mixture	Re_λ	Re_l	u'_{rms}/S_L	l/δ_F	D/δ_F
HR37LL	H_2–air	37.4	144	0.85	169	44.1
HR37MM	H_2–air	37.4	144	1.70	84.3	30.3
HR37HS	H_2–air	37.4	144	3.41	42.2	17.9
HR60HM	H_2–air	60.8	203	3.39	90.1	18.7
HR97HM	H_2–air	97.1	515	5.78	122	10.6
MR37HS	CH_4–air	37.4	144	5.80	24.7	5.69

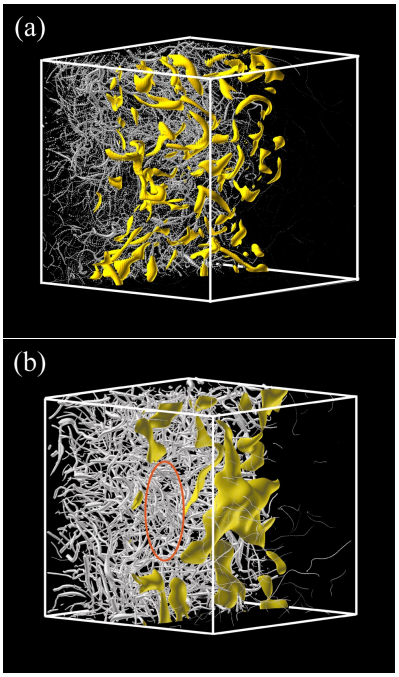

Figure 1: Contour surfaces of heat release rate with the axes of the coherent fine scale eddy for HR97HM (a) and MR37HS (b).

Local Flame Structure of Turbulent Premixed Flames

Figure 1 shows contour surfaces of the heat release rate with the axes of the fine scale eddy for HR97HM and MR37HS. The contour level of the heat release rate is $\Delta H/\Delta H_L \geq 1.0$, where ΔH_L denotes the maximum heat release rate of the laminar flame. The thickness of the axis is drawn to be proportional to the square root of the second invariant of the velocity gradient tensor on the axis. The second invariant is normalized by u'_{rms} and η in the unburned side. A thicker eddy shows stronger swirling motion around the eddy. Note that the most expected diameter of these fine scale eddies is 8η and the maximum azimuthal velocity reaches to $3 \sim 4u'_{rms}$ (Tanahashi et al., 2001). The number density of the fine scale eddies in the unit volume of the integral length scale (l^3) increases with the increase of Re_λ (Tanahashi et al., 2000b). For high Reynolds number hydrogen-air turbulent premixed flames, the wrinkling of the flame surfaces also increases and appearance of 3D structure increases because of high probability of the fine scale eddies which possess azimuthal velocity faster than S_L (Tanahashi et al., 2004b).

Differences between hydrogen-air and methane-air turbulent premixed flames can be observed in distribution of the heat release rate. In Fig. 1(b), there is a large region of low heat release rate (see circle in Fig. 1(b)). This has never been observed in hydrogen-air turbulent premixed flames. The low heat release rate area shows about $0.3\Delta H_L$ although

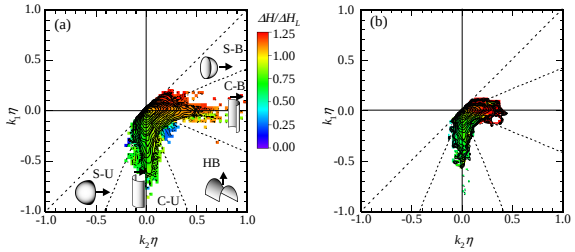

Figure 2: Joint probability density functions of principal curvatures of flame front with conditional mean local heat release rate for HR60HM (a) and MR37HS (b).

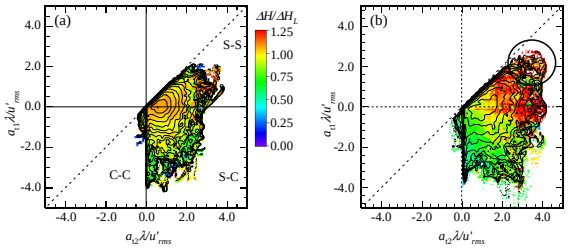

Figure 3: Joint probability density functions of the minimum and maximum strain rate with conditional mean local heat release rate for HR60HM(a) and MR37HS(b).

temperature is relatively uniform and still high. This region may represent the local extinction in turbulent premixed flames.

Statistical Characteristics of Local Flame Structure

To clarify effects of turbulence characteristics on local flame structure quantitatively, statistical characteristics of flame elements are investigated. The flame fronts are defined as points with the local maximum temperature gradient. In the case of hydrogen-air turbulent premixed flames, the maximum heat release rate increases with the increase of turbulence intensity or the decrease of turbulence length scale, and reaches to $1.3\Delta H_L$ at the same Reynolds number. The variance of local heat release rate in methane-air turbulent premixed flame is much larger than those in hydrogen-air flames, and there are lots of flame elements that show high heat release rate of $2.0\Delta H_L$ and low heat release rate of $0.5\Delta H_L$ along the flame front. For hydrogen-air flames, pdfs of the local heat release rate show their peaks at about $1.0\Delta H_L$. For methane-air flame, however, pdf shows a weak peak at $0.7\Delta H_L$.

The correlation between local heat release rates and geometrical shapes of flame front is examined by using principal curvatures (k_1 and k_2)(Tanahashi et al., 2004b; Tanahashi et al., 2005a). Principal curvatures are defined as $k = k_1 + k_2 (k_1 < k_2)$, where k denotes mean curvature. Figure 2 shows the joint pdfs of principal curvatures of flame front with conditional mean local heat release rate for HR60HM and MR37HS. The flame elements convex toward the burned side are defined to have positive value and the principal curvatures are normalized by η. From two principal curvatures, flame shape can be classified into spherical surface convex toward the burned side (S-B), cylindrical surface convex toward the burned side (C-B), hyperboloidal surface (HB), cylindrical surface convex toward the unburned side (C-U) and spherical surface convex toward the unburned side (S-U). The conditional mean local heat release rate is shown in Fig. 2 by colors. For hydrogen-air flames, number of flame elements in C-B and S-B regimes increases with the increase of Re_λ. Flame elements in S-B attribute to the spire and handgrip structures (Nada et al., 2004), and those in C-B regime are mainly created by fine scale eddies parallel to the flame front. C-B and S-B flame elements would dominate the total heat release rate and the turbulent burning velocity in high Reynolds number hydrogen-air premixed flames. Heat release rates tend to increase when the regime changes from S-U to S-B as shown in Fig. 2(a), while the correlation between heat release rate and curvatures for methane-air premixed flame is not clear compared with hydrogen-air cases.

The strain rate tangential to the flame front has been discussed by $a_t = \boldsymbol{t}_1\boldsymbol{t}_1 : \nabla\boldsymbol{u} + \boldsymbol{t}_2\boldsymbol{t}_2 : \nabla\boldsymbol{u}$, where $\boldsymbol{t}_1$ and $\boldsymbol{t}_2$ represent unit vectors tangential to the flame front and are satisfying a relation of $\boldsymbol{t}_1 \cdot \boldsymbol{t}_2 = 0$ (Candel and Poinsot, 1990). Here, the minimum and the maximum strain rate on the flame surface are introduced to investigate strain rate effect correctly (Tanahashi et al., 2004b; Tanahashi et al., 2005a). Figure 3 shows joint pdfs of the minimum and maximum strain rate with conditional mean local heat release rate for HR60HM and MR37HS. a_{t1} and a_{t2} denote the minimum and maximum strain rates and are normalized by u'_{rms}/λ. The tangential strain rate on the flame surface can be classified into three types; stretching in the two directions (S-S), stretching and compression in each direction (S-C), and compression in two direction (C-C). The most expected strain field is simple 2D strain rate of the order of u'_{rms}/λ ($a_{t1} \approx 0$ and $a_{t2} \approx u'_{rms}/\lambda$). For both fuels, the flame elements in S-S regime are more than 50% and almost all of flame elements are under the stretching in one direction at least. Flame elements in C-C regime are scarcely observed and number of flame element in S-C regime increases with the increase of Re_λ. Note that flame elements in S-S regime could be approximated by laminar flames observed in counter-flow flame, whereas it is not the case for those in S-C regime.

For hydrogen-air flames, correlations between heat release rates and tangential strain rates are hardly observed. However, for methane-air flame, they show relatively strong correlation. The heat release rates tend to increase from C-C regime to S-S regime. In S-S regime, the heat release rate also increases with the increase of the tangential strain rate. However, in S-S regime, the flame elements that are stretched strongly in two directions (see circle in Fig. 3(b)) tend to show low heat release rate. Most of these flame elements exist in the vicinity of low heat release rate region in Fig. 1(b) and they are considered to be closely related to local extinction of turbulent premixed flames.

IGNITION AND PROPAGATION OF TURBULENT PREMIXED FLAME

DNS of ignition and propagation of hydrogen-air premixed flame in 2D and 3D homogeneous isotropic turbulence have been conducted to investigate effects of turbulence on the ignition and propagation process (Terakado et al., 2007). A detailed kinetic mechanism is used to represent hydrogen-air reaction in turbulence. The governing equations are solved by using a fourth order central finite difference scheme. Navier-Stokes Characteristic Boundary Condition (NSCBC) (Poinsot and Lele, 1992) is assumed in all directions.

As an initial condition, high temperature region is given at the center of computational domain as an ignition kernel. A hydrogen-air mixture is assumed to be uniform at 0.1MPa for all cases. Numerical parameters of DNS are listed in Table 2. To investigate the Reynolds number effects on the

Table 2: Numerical parameters of DNS of ignition and propagation of premixed flame in turbulence.

	ID	ϕ	Re_λ	Re_l	u'_{rms}/S_L	l/δ_F	l/δ_L	$L_x \times L_y (\times L_z)$	$N_x \times N_y (\times N_z)$
2D	Case1	1.0	47.1	134.8	0.77	174.3	3.04	10×10mm	1025×1025
	Case2	1.0	66.4	170.6	1.93	88.2	1.54	15×15mm	1537×1537
	Case3	1.0	79.1	150.3	1.93	78.0	1.36	10×10mm	1025×1025
	Case4	1.0	106.8	320.1	1.92	166.7	2.91	10×10mm	1025×1025
	Case5	0.8	106.8	320.1	2.02	158.4	2.83	10×10mm	1025×1025
	Case6	0.6	106.8	320.1	2.27	141.0	2.77	10×10mm	1025×1025
3D	Case7	1.0	60.8	203	1.52	131	2.28	7×7×7mm	385×385×385
	Case8	0.6	60.8	203	1.80	111	2.17	7×7×7mm	385×385×385

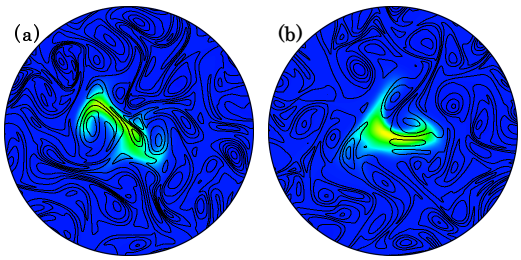

Figure 4: Distributions of temperature and vorticity in induction phase for case3-1 (a) and case3-2 (b) ($t/\tau_F = 0.412$).

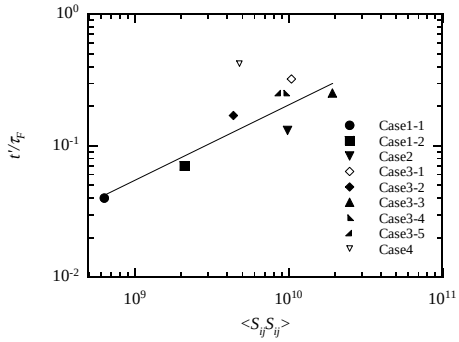

Figure 5: Relation between ignition delay and mean strain rate.

ignition and propagation process, DNS are conducted with four different Reynolds number for 2D cases. In 2D cases, to clarify the relation between the local structure of turbulence and ignition process, the mixture is ignited from different region in the statistically same turbulent field. 3D cases are also calculated for different equivalence ratio. In the turbulent combustion diagram by Peters (1999), Case1 is classified in wrinkled flamelets. Other cases are classified in corrugated flamelets. For comparison, laminar conditions are also calculated.

Effects of Turbulence on Ignition

For the ignition of hydrogen-air mixture, amount of H atom is very important. For high turbulence intensity case, H atom distribution is strongly distorted by the eddy and H atoms which are transported into low temperature regions disappear. In these regions, productions of intermediates through H atom are suppressed. Ignition delay is assumed as period until getting to thermal runaway. Thermal runaway is defined as inflection point of temperature in rapid rise of the maximum temperature. The temperature for high turbulence intensity case decreases in the induction phase particularly, and the ignition delay is more than twice of the laminar case. The ignition delay tends to increase with turbulence intensity. However, it should be noted that the ignition delay is different even for the same turbulent flow fields if the ignition point was different. Figure 4 shows distributions of temperature and vorticity in the induction phase for case3 with different ignition point. The high temperature region is stretched by eddies in a different way for each case. The temporal developments of maximum temperature show that the ignition delay is different even if the turbulent field is statistically same. Therefore, the ignition delay significantly depends on local characteristics of turbulence. Figure 5 shows relation between the ignition delay and mean strain rate. Mean strain rate represents an average of strain rate in the region of initial ignition kernel. The ignition delay tends to increase with increase of mean strain rate except for case3-1 and case4, and can be approximated as $t'/\tau_F \propto \langle S_{ij}S_{ij}\rangle^{0.57}$. In case3-1 and case4, the flames are ignited from several points since the initial high temperature region is separated by eddies as shown below.

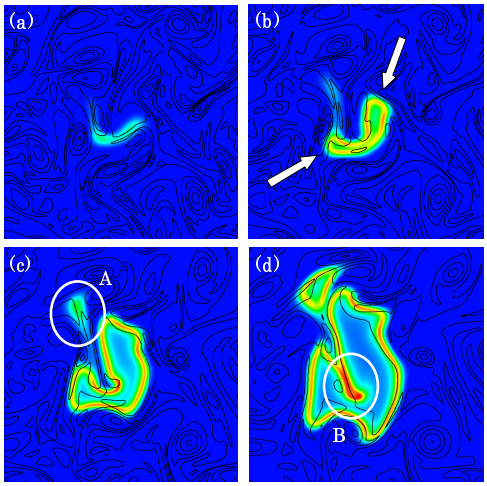

Figure 6: Temporal developments of distributions of heat release rate and vorticity in propagation process for case4 ((a) $t/\tau_F = 0.74$, (b) $t/\tau_F = 1.07$, (c) $t/\tau_F = 1.40$, (d) $t/\tau_F = 1.73$).

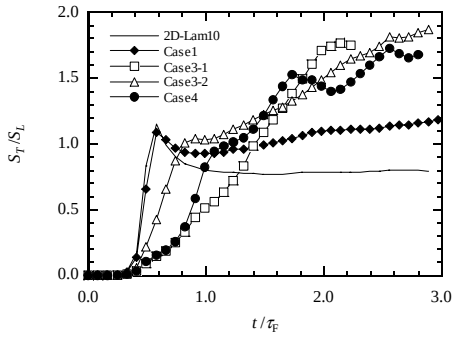

Figure 7: Temporal developments of the turbulent burning velocity for 2D-Lam10, case1, case3-1, case3-2 and case4.

Effects of Turbulence on Propagation

Figure 6 show the temporal developments of distributions of heat release rate and vorticity in propagation process for case4. The heat release rate is normalized by the maximum

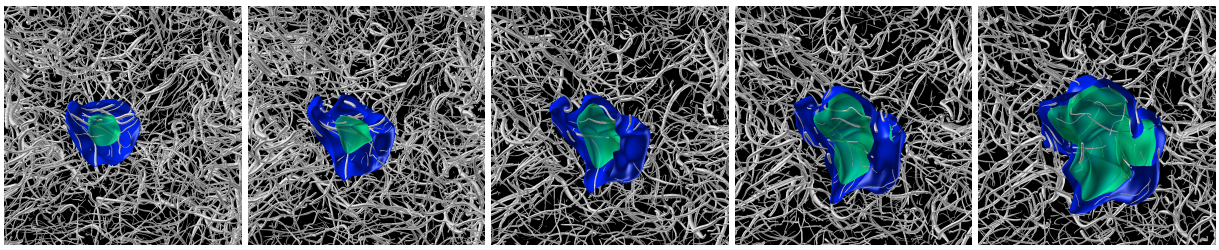

(a) $t/\tau_F = 0.165$ (b) $t/\tau_F = 0.412$ (c) $t/\tau_F = 0.659$ (d) $t/\tau_F = 0.907$ (a) $t/\tau_F = 1.15$

Figure 8: Temporal developments of contour surfaces of temperature and axes of coherent fine scale eddy for case7.

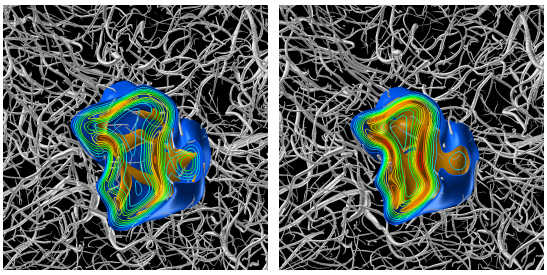

(a) Case7 (b) Case8

Figure 9: The contour surfaces of heat release rate and axes of coherent fine scale eddy in propagation process ((a)$t/\tau_F = 1.15$, (b)$t/\tau_F = 0.837$).

heat release rate of freely propagating one-dimensional laminar flame. The flame propagates along the edge of eddies as shown by allows in Fig. 6(b). The high temperature region which is separated from the initial ignition kernel in the induction phase is ignited later than the ignition in main kernel (see the circle A). This result suggests that multiple points ignition with different timing may occur even for an initial ignition kernel in turbulence. Furthermore, as shown by the circle B, the heat release rate reaches over $1.2\Delta H_L$ at the flame fronts that are enclosed by the burnt gas and that are convex toward the burnt side. The high heat release rate of these flame fronts has also been reported by previous studies on statistically-planer turbulent premixed flame propagating in homogeneous turbulence (Tanahashi et al., 2000a).

These characteristics of the flame structure are reflected in turbulent burning velocity. Figure 7 shows the temporal developments of turbulent burning velocity for several cases. The turbulent burning velocity is normalized by the laminar burning velocity of one-dimensional planer flame. Except for low Reynolds number case (case1), it is apparent that temporal developments of turbulent burning velocity show different trends compared with the laminar case. The burning velocity in case4 shows the rapid rise at about $t/\tau_F = 1.7$, which is caused by appearance of flame elements with high heat release rate as mentioned previously (circle B in Fig. 6(d)). In case3-1, the ignition takes place from three points with different timing, while the ignition in case3-2 takes place only from one point. Therefore, temporal developments of the turbulent burning velocity for these cases are different.

Three Dimensional Effects

Figure 8 shows temporal developments of contour surfaces of temperature and axes of coherent fine scale eddy for 3D case. Blue surfaces represents $T = 830$K and green does $T = 1200$K. The coherent fine scale eddy changes the shape of the initial high temperature region. Although coherent fine scale eddies are weakened in high temperature burnt gas, dilatation effects of the fluid (not shown here) scarcely affect the fine scale eddies around the flame. The flame front tends to propagate between coherent fine scale eddies. Near the coherent fine scale eddy, flame front seems to be deformed significantly. As the dilatation effects are relatively weak, the local flame structure is dominated by the strain rate due to the turbulent motion. In the induction phase, dependence on the equivalence ratio is week similar to 2D cases and the ignition delay is elongated for the turbulent cases. However, since the initial maximum temperature of the ignition kernel is set to be higher than that of 2D cases, the ignition delay is not so significant compared with the 2D cases. This is the decrease of relative importance of turbulent convection (or turbulent heat flux) for the ignition delay. In Fig. 5, the ignition delay shows strong correlation with the mean strain rate in the ignition kernel. The order of the strain rate is about $10^{10}\mathrm{s}^{-1}$ for the 2D cases. One may feel that the magnitude of the strain rate is too high. However, in real 3D turbulence, strain rate is higher. Note that strain rate in turbulence can be estimated as $\mathrm{O}(u'_{rms}/l)$ for 2D turbulence and $\mathrm{O}(u'_{rms}/\lambda)$ for 3D one. Therefore, strain rate becomes higher for 3D turbulence with the same turbulence intensity and same integral length scale.

Figure 9 shows the contour surfaces of heat release rate with axes of coherent fine scale eddy in the propagation process for case7 and case8. Here, the blue surfaces represents $0.1\Delta H_L$ and yellow ones does $1.0\Delta H_L$. On a cross section, contour lines of heat release rate are shown with the interval of $0.1\Delta H_L$. For $\phi = 1.0$ (case7), the heat release rate shows high value in the flame region convex toward burnt side similar to the 2D cases. Due to the presence of the coherent fine scale eddy, the high heat release rate region shows a slender filament-like structure. In contrast, the heat release rate for $\phi = 0.6$ (case8) is independent of the flame geometry and shows relatively high value which exceeds $1.2\Delta H_L$.

SIMULTANEOUS CH-OH PLIF AND STEREOSCOPIC PIV FOR INVESTIGATION OF LOCAL FLAME STRUCTURE

In this section, simultaneous CH-OH PLIF and stereoscopic PIV measurement, which was developed in our previous study (Tanahashi et al., 2005b), are used to clarify the relation between the local flame structure and the turbulence characteristics in turbulent premixed flames. The curvature of flame fronts and tangential strain rate at the flame fronts obtained by the simultaneous measurements are compared directly with those obtained by 3D DNS of hydrogen-air and methane-air turbulent premixed flames (Tanahashi et al., 2000a; 2002; Nada et al, 2004; Kikuta et al., 2004).

Experimental Method

The schematic diagram of the experimental setup for simultaneous CH-OH PLIF and stereoscopic PIV measurement is shown in Fig. 10. Details of the experimental setup can be found in Tanahashi et al., (2005b). An in-

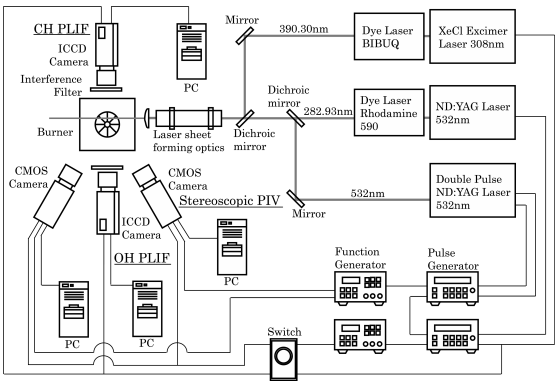

Figure 10: Schematic of the simultaneous CH-OH PLIF and stereoscopic PIV measurement.

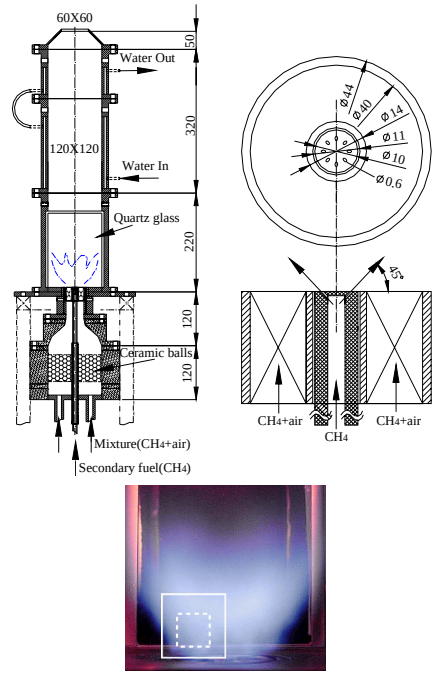

Figure 11: Swirl-stabilized burner and direct photograph of turbulent premixed flame for Q=300L/min and ϕ=1.0.

tensified CCD camera (Andor Technology, DH734-25U-03, 1024×1024 pixels) with a Micro-Nikkor 105mm/f2.8 lens was used for the imaging of CH. Second intensified CCD camera (PI-MAX, 512RB-G1, 512×512 pixels) with an UV-Nikkor 105mm/f4.5 lens was used for the imaging of OH. This camera is located on the opposite side of the burner from the intensified CCD camera for CH. For PLIF, the laser beam is shaped into 200μm thickness vertical sheet with 30mm height. The CH-OH PLIF system affords a view of 30mm × 30mm. Therefore, spatial resolution of PLIF is 30μm×30μm×200μm for CH and 60μm×60μm×200μm for OH. To optimize signal-to-noise ratio, image intensifier gate time was set to 30ns. For the stereoscopic PIV, the measuring region and the interrogation region are set to 14.3mm×14.3mm and 24×24 pixels, respectively. Since the thickness of the laser sheet is about 1.0mm, spatial resolution of the PIV becomes 670μm×670μm×1000μm. As for the tracer particles, 0.18μm Al_2O_3 are used.

CH and OH PLIF are synchronized to $\Delta t/2$ after the first laser pulse for PIV, where Δt is the time interval of PIV measurement. Time difference error between PLIF and PIV is limited to be less than 100ns, and that between CH PLIF and OH PLIF is controlled to be of the order of 1ns.

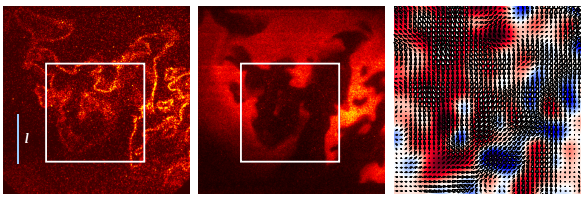

Figure 12: CH (left) and OH (center) fluorescence images and three-component velocity map (right) (Re_λ=115.0, ϕ =1.0).

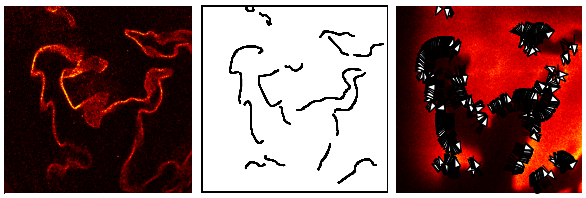

Figure 13: CH fluorescence image (left), detected flame front (center) and OH fluorescence image with unit vectors normal to the flame front (right).

Based on the characteristics of the turbulent flow field, Δt is set to 15μs.

Figure 11 shows the schematics of the swirl-stabilized burner (Tanahashi et al., 2005b) and a direct photograph of methane-air turbulent premixed flame at stoichiometric condition with flow rate Q = 300L/min. On each side of combustion chamber, a silica glass plate was installed to allow optical access. The swirl nozzle has swirl vanes of 14mm inner diameter and 40mm outer diameter with inclination of 45 degree from the nozzle axis. Although a secondary fuel nozzle was mounted at center of the swirl vanes, this nozzle was not used in the present study. In this experiment, horizontal and vertical direction of the laser sheet is defined as the x and y axis respectively. The z axis is selected to be normal to the laser sheet.

The simultaneous CH-OH PLIF and stereoscopic PIV are conducted for three different flow rates: Q = 200, 250 and 300L/min, and for four different equivalence ratios: ϕ = 1.0, 0.9, 0.8, 0.7. Measurements were conducted in a cross-section with the maximum u'_{rms}. White box in the direct photograph denotes the measurement region of CH and OH PLIF, and box with broken lines represents the measurement region of PIV. The turbulence characteristics obtained by the hot-wire measurement were shown in Table 3. With the increase of the flow rate, Re_λ changes from 63.1 to 115.0. All conditions are classified near the boundary between corrugated flamelets and thin reaction zones in the turbulent combustion diagram.

Direct Comparison of Experiment and DNS

CH and OH distributions and 3C velocity map obtained for Re_λ = 115.0 and ϕ = 1.0 are shown in Fig. 12. The area denoted by a white box in the CH and OH images corresponds to the measurement region of the stereoscopic PIV. In CH and OH images, red color represents high concentration and a white line does integral length scale of turbulence. In the velocity map, the x and y components are shown by arrows and the z component is represented by color. The velocity from behind to front has positive value and is denoted by red. As shown in our previous study (Tanahashi et al., 2005b), flame fronts have large-scale wrinkling of the order of the integral length scale and small-scale wrinkling less than the Taylor micro scale. In this study, flame front was determined from CH PLIF image and a unit vector nor-

Table 3: Experimental conditions of simultaneous CH-OH PLIF and stereoscopic PIV.

Q[l/m]	Re_l	Re_λ	u'_{rms}[m/s]	l[mm]	λ[mm]	η[mm]	l/δ_F	u'_{rms}/S_L
200	265.8	63.1	1.24	3.42	0.812	0.0575	41.7∼82.9	3.20∼6.42
250	602.0	95.0	1.59	6.02	0.950	0.0548	73.3∼146.0	4.12∼8.23
300	881.0	115.0	1.92	7.27	0.949	0.0498	88.6∼176.6	4.99∼9.95

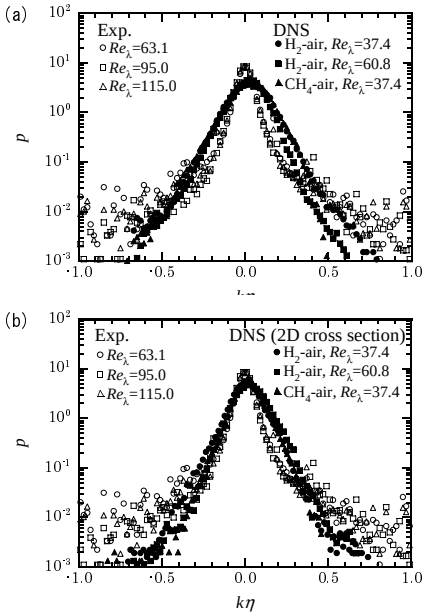

Figure 14: Probability density functions of the curvature of the flame front obtained by the present experiment (ϕ=1.0) and DNS. For DNS, the curvature is calculated from 3D surface in (a) and 2D cross section in (b).

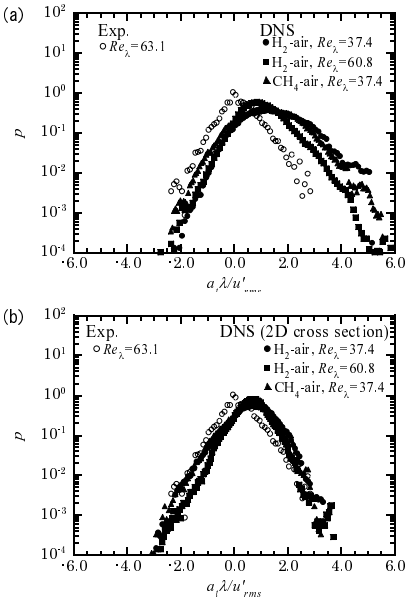

Figure 15: Probability density functions of the tangential strain rate obtained by the present experiment (ϕ=1.0) and DNS. For DNS, the tangential strain rate is calculated from 3D velocity distribution in (a) and 2C velocity distribution on 2D cross section in (b).

mal to the flame front was estimated from the gradients of OH at the flame front, as shown in Fig. 13. The curvature is estimated from the flame normal vectors and defined to be positive for flame elements convex toward the burned side.

In Fig. 14(a), probability density functions (pdf) of the curvature obtained by the experiment are compared with the results of 3D DNS (Kikuta et al, 2004; Nada et al., 2004). Note that the curvature of the flame front for DNS represents mean value defined by $k = k_1 + k_2$. The curvature is non-dimensionalized by η. The maximum values of $|k\eta|$ are about 1.0 both for the experiment and DNS. Therefore, the minimum radius of curvature is Kolmogorov length. However, the shapes of the pdf by the experiments are slightly different from those by DNS. This is caused by the curvature estimation only from 2D cross section in the experiments. In Fig. 14(b), the experimental results are compared with the curvature calculated from 2D cross section of DNS. In the negative portion of the pdf, the experimental results coincide with DNS results very well. In the positive portion, however, difference between the experiment and DNS still remains. This discrepancy might be due to the difference of the turbulent flow field; homogeneous isotropic turbulence for DNS and turbulent swirling flow for the experiment.

From the PIV measurement, tangential strain rate at the flame front is evaluated for $Re_\lambda = 63.1$ and $\phi = 1.0$. In Fig. 15(a), tangential strain rates obtained from 2C velocity on the x-y plane are compared with those by DNS. Similar to the curvature, tangential strain rates for DNS are calculated from 3D and 3C velocity distribution. The tangential strain rate is non-dimensionalized by Taylor time scale. The magnitude of the strain rate is of the order of the Taylor time scale both for the experiment and DNS. However, pdf obtained by the experiment shift into the negative portion compared with those by DNS. In Fig. 15(b), pdfs of the tangential strain rate which are evaluated from 2D cross section of the DNS results are presented. The experimental results become close to the DNS results. These facts suggest that 3D and 3C velocity measurements such as dual-plane stereoscopic PIV and holographic PIV are required to investigate tangential strain rate at the flame front correctly.

CH DOUBLE-PULSED PLIF FOR DIRECT MEASUREMENT OF FLAME DISPLACEMENT

CH double-pulsed PLIF has been developed to evaluate flame displacement speed in turbulent premixed flames (Tanahashi et al., 2006a). The developed time-resolved CH PLIF is applied to relatively high Reynolds number turbulent premixed flames, and dynamics of local flame structures are discussed.

Experimental Setup

The schematic diagram of the experimental setup for CH double-pulsed PLIF measurement is shown in Fig. 16. By combining two independent CH PLIF systems, the time-resolved PLIF system is comprised. Laser beams from each laser systems are polarized in vertical and horizontal direction and are lead to same optical pass by a polarizing beam splitter. The combined beams are expanded into laser sheets by laser sheet forming optics. Fluorescence from excited CH radicals are detected by two intensified CCD cameras (Andor Technology, iStar DH734-25U-03, 1024 × 1024 pixels) fitted with 105 mm f2.8 lens (Nikon, Micro-nikkor) and an optical filter (SCHOTT, KV418). These cameras are located on the opposite side of the burner, and optical axes are set to

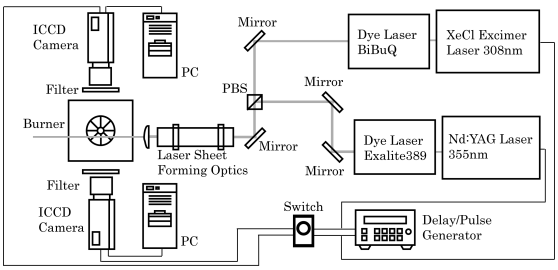

Figure 16: Schematic diagram of the CH double-pulsed PLIF measurement.

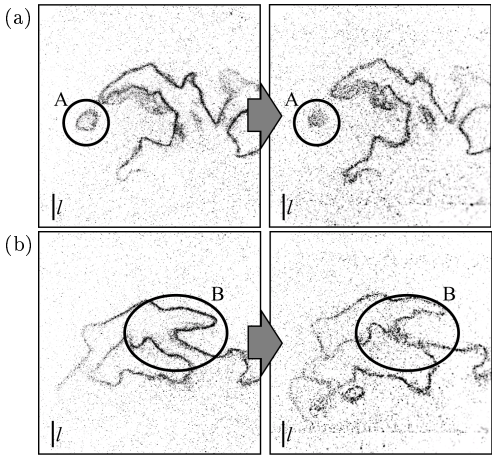

Figure 17: CH double-pulsed fluorescence images of CH_4-air turbulent premixed flames ($\phi = 1.0$, $Re_\lambda = 63.1$, (a):Δt = 100 μs, (b):Δt = 200 μs).

be perpendicular to the laser sheet. Time interval Δt of successive PLIF could be selected arbitrarily. In this study, Δt is set to the range of 30 to 200 μs. The laser beam is shaped into 200 μm thickness vertical sheet with 30 mm height. Each camera afford a view of 30 mm $\times$ 30 mm. Therefore, spatial resolution of PLIF is 30μm $\times$ 30μm $\times$ 200μm. CH double-pulsed PLIF measurements are conducted in the swirl-stabilized combustor shown in the previous section for three different flow rates; Q = 200, 250 and 300 L/min, at stoichiometric condition.

Dynamics of Flame Front in Turbulence

Typical successive CH fluorescence images for Re_λ = 63.1 (Q = 200 L/min) are shown in Fig. 17 for two different realizations. Time interval of successive CH PLIF are 100 μs for Fig. 17 (a) and 200 μs for (b), and each image shows 30 mm $\times$ 30 mm regions. In these figures, black line represents the integral length scale of turbulence. Flame front represented by high concentration CH layer shows very complicated distribution and have several sizes of wrinkling; large-scale more than integral length scale to small-scale less than Taylor micro scale (Tanahashi et al., 2005b).

In addition to these instantaneous features of flame front, dynamics of flame front can be discussed from the successive flame front images. As shown in Fig. 17, ring-like flame fronts are found in the first images (see circle A). The size of these flame fronts is diminished or they disappear in the second images. Isolating process of unburned mixture from main flame front are also observed as denoted by a circle B in Fig. 17. The size of isolating flame is of the order of or larger than the integral length of turbulence. These deformations of flame front might represent the burning and generating process of the unburned mixture in burnt gas or the handgrip

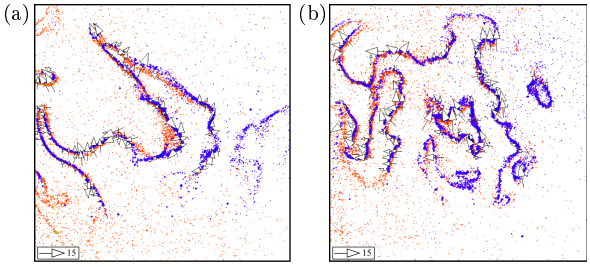

Figure 18: Successive CH fluorescence images and vector maps of flame displacement speed (red: 1st image, blue: 2nd image, (a):Re_λ = 63.1 and (b):Re_λ = 115.0).

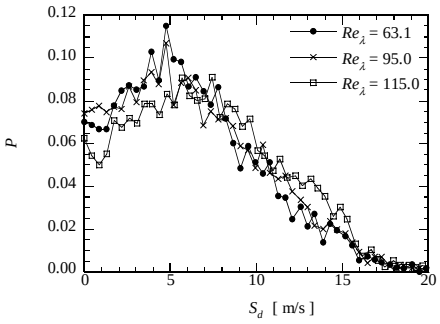

Figure 19: Probability density functions of the flame displacement speed.

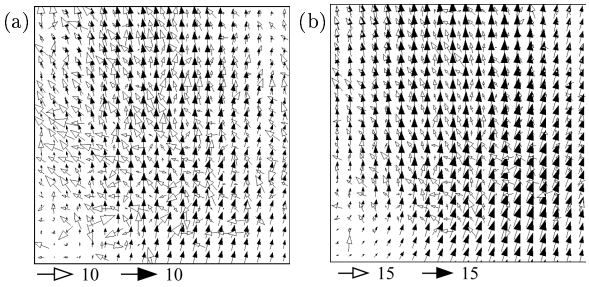

Figure 20: Vector maps of mean flame displacement speed (white arrows) and mean fluid velocity (black arrows), (a):Re_λ = 63.1 and (b):Re_λ = 115.0.

structure (Nada et al., 2004) which has been shown by 3D DNS of turbulent premixed flames. The generation of these isolating flames has important roles in the enhancement of turbulent burning velocity.

Direct Measurement of Flame Displacement Speed

In this study, from successive CH fluorescence images, flame displacement speed is evaluated (Tanahashi et al., 2006a). Figure 18 shows vector map of flame displacement speed with successive CH fluorescence images. In these figures, red and blue color represents 1st and 2nd CH fluorescence image, respectively. White vectors represent the local flame displacement speed. Directions of the flame displacement vectors coincide very well with observations from the successive CH fluorescence images. With the increase of Reynolds number, flame geometry becomes complex and small wrinkles of the flame front increase. The displacement direction is different for the small wrinkles, and then flame shape is distorted.

Flame Displacement Speed of Turbulent Premixed Flame

In Fig. 19, pdfs of local flame displacement speed S_d are presented. To obtain these results, 120 sets of successive CH images and more than 5000 displacement vectors

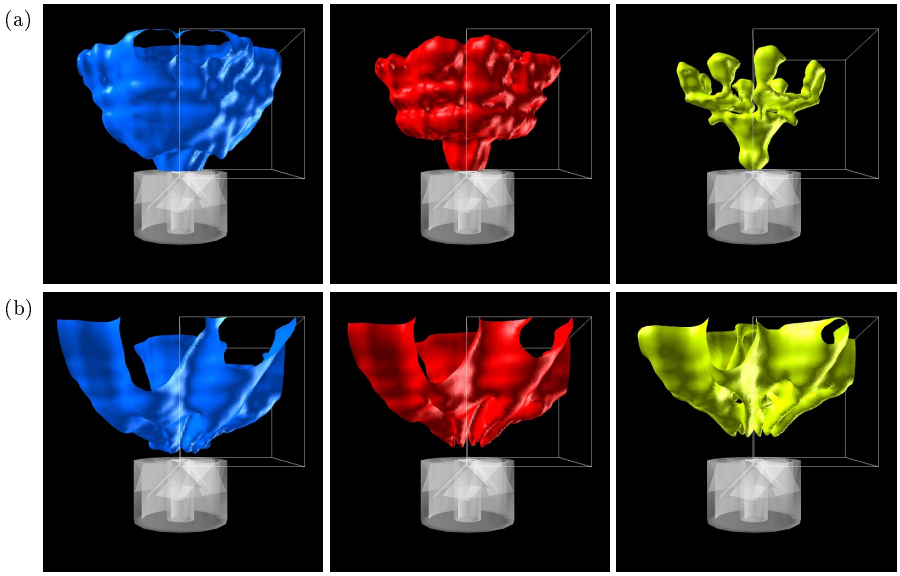

Figure 21: 3D distribution of probability of flame front existence (30% in unburnt side, 50% and 30% in burnt side from the left) for no control case (a) and continuous secondary fuel injection case (b).

are used for each condition. The probability for high displacement speed shows a little bit high for large Reynolds number case. Mean fluid velocity in the present measurement region has been measured by stereoscopic PIV in our previous study (Tanahashi et al., 2005b). The mean velocity and turbulence intensity increase with the increase of Reynolds number. Typical values are about 5.0 m/s to 8.9 m/s for mean streamwise velocity and about 2.5 m/s to 3.6 m/s for turbulence intensity. Although the velocity field depends on Reynolds number significantly, flame displacement speed is slightly affected by Reynolds number. These results reflect the correctness of the flamelet concept, because the turbulent burning velocity increases due to the increase of flame surface area and the flame displacement speed is not modified significantly.

In Fig. 20, mean flame displacement vectors are compared with the mean fluid velocity vectors obtained from previous study (Tanahashi et al., 2005b). With the increase of Reynolds number, the mean flame displacement vectors tend to align with the mean fluid velocity vectors. These results suggest that effects of convection become strong for high Reynolds number case. Even for the highest Reynolds number case, misalignment still remains, which might be caused by the sampling number for the present displacement speed. However, this misalignment will be explained by the simultaneous CH double-pulsed PLIF and stereoscopic PIV, which gives flame displacement speed, flame curvature and the strain rate simultaneously, in the near future.

RECONSTRUCTION OF 3D FLAME STRUCTURE BY MULTIPLE-PLANE OH PLIF

As an application of laser diagnostics for developments of combustors, reconstruction of 3D flame structure based on multiple-planes OH PLIF (Tanahashi et al., 2006b) is presented in this section. From the results of OH PLIF on 25 different planes of the swirl-stabilized combustor shown in Fig. 11, 3D flame structure has been reconstructed to investigate relations between the flame structure and combustion noise. Since a quarter of the combustor is the same structure as the other quarters statistically, 3D flame structure is reconstructed by considering the rotational symmetry of the combustor (Tanahashi et al., 2006b). The reconstructed 3D structures are shown in Fig. 21. The present swirl-stabilized combustor can be controlled by secondary fuel injection. It has been shown that combustion noise of 110dB for no control case can be reduced to 100dB by continuous secondary fuel injection (Tanahashi et al., 2006b). The contour surfaces in Fig. 21 represent 30% probability of flame existence in unburnt side, 50% and 30% in burnt side. Note that fluctuation of the flame front is main sound source in the turbulent combustion field.

The 3D flame structure is significantly affected by the secondary fuel injection. Near the inlet, the 50% region is tight and expands drastically in the downstream for the no control case. Note that this slender neck near the inlet does not mean the stability of the recirculation zone. Fluctuation of the high-temperature fluid in the recirculation zone is high for the no control case, which results in the fact that contour surfaces of three probabilities have different shapes in Fig. 21. Compared with the no control case, contour surfaces of three probabilities are similar shapes for secondary fuel injection case, which means that secondary fuel injection suppresses the fluctuation of high-temperature fluid in the recirculation zone. In the flame zone, fluctuation of the flame front is high for no control case (flame brush is wide). For the secondary fuel injection case, the flame zone spreads into the outside and flame brush becomes thin. The regions with the flame front are pushed up by the jets of the secondary fuel, and no flame regions intrude into the downstream. The 3D structures for this case reflect effects of the secondary fuel clearly. Expansion of the 50% area does not mean the increase of the flame front fluctuation.

These results are very useful to control the turbulent combustion noise, and give a reference experimental data for validation of numerical simulations, especially large eddy simulation, of turbulent combustion.

SUMMARY

In this paper, recent 3D DNS and advanced laser diagnostics of turbulent premixed flame are summarized. The combination of various measurement techniques such as PLIF and PIV will give more detailed experimental data which have high accuracy enough to compare with DNS. The direct comparisons between experiment and DNS lead

to deep insight into the turbulent combustion, and to the development of high efficient and low emission combustors.

ACKNOWLEDGEMENTS

This work is partially supported by Grant-in-Aid for Scientific Research (A) (No.15206023) and (S) (No.18106004) of Japan Society for the Promotion of Science and by Grant-in-Aid for Young Scientists (A) (No.16686011) of the Ministry of Education, Culture, Sports, Science and Technology, Japan.

REFERENCES

Allen, M., Howe, R. D., and Hanson, R. K., 1986, *Opt. Lett.*, Vol. 11, pp. 126-128.

Arroyo, M. P., and Greated, C. A., 1991, *Meas. Sci. Technol.*, Vol. 2, pp. 1181-1186.

Baum, M., Poinsot, T. J., Haworth, D. C., and Darabiha, N., 1994, *J. Fluid Mech.*, Vol. 281, pp. 1-32.

Bell, J. B., Day, M. S., and Grcar, J. F., 2002, *Proc. Combust. Inst.*, Vol. 29, pp. 1987-1993.

Bockle, S., Kazenwadel, J., Kunzelmann, T., Shin, D.-I., Schulz, C., and Wolfrum, J., 2000, *Proc. Combust. Inst.*, Vol. 28, pp. 279-286.

Candel, S. M., and Poinsot, T. J., 1990, *Combust. Sci. Technol.*, Vol. 70, pp. 1-15.

Carter, C. D., Donbar J. M., and Driscoll, J. F., 1998, *Appl. Phys. B*, Vol. 66, pp. 129-132.

Clavin, P., 1985, *Prog. Energy Combust. Sci.*, Vol. 11, pp. 1-59.

Donbar, J. M., Driscoll, J. F., and Carter, C. D., 2000, *Combust. Flame*, Vol. 122, pp. 1-19.

Dyer, M. J., and Crosley, D. R., 1985, *Proc. Int. Conf. Lasers*, Vol. 84, pp. 211-218.

Echekki, T., and Chen, J. H., 1996, *Combust. Flame*, Vol. 106, pp. 184-202.

Hanson, R. K., 1986, *Proc. Combust. Inst.*, Vol. 21, pp. 1677-1691.

Haworth, D. C., and Poinsot, T. J., 1992, *J. Fluid Mech.*, Vol. 244, pp. 405-436.

Jenkins, K. W., and Cant, R. S., 2002, *Proc. Combust. Inst.*, Vol. 29, pp. 2023-2029.

Kalt, P. A. M., Frank, J. H., and Bilger, R. W., 1998, *Proc. Combust. Inst.*, Vol. 27, pp. 751-758.

Kaminski, C. F., Hult, J., and Alden, M., 1999, *Appl. Phys. B*, Vol. 68, pp. 757-760.

Kido, H., Nakahara, M., Nakashima, K., and Hashimoto, J., 2002, *Proc. Combust. Inst.*, Vol. 29, pp. 1855-1861.

Kikuta, S., Tanahashi, M., and Miyauchi, T., 2004, *Proc. 42nd Symp. (Japanese) Combust.*, pp. 355-356.

Kothnur, P. S., Tsurikov, M. S., Clemens, N. T., Donbar, J. M., and Carter, C. D., 2002, *Proc. Combust. Inst.*, Vol. 29, pp. 1921-1927.

Kychakoff, G., Paul, P. H., van Cruyningen, I., and Hanson, R. K., 1987, *Appl. Opt.*, Vol. 26, pp. 2498-2500.

Law, C. K., and Sung, C. J., 2000, *Prog. Energy Combust. Sci.*, Vol. 26, pp. 459-505.

Mansour, M. S., Peters, N., and Chen, Y. C., 1998, *Proc. Combust. Inst.*, Vol. 27, pp. 767-773.

Nada, Y., Tanahashi, M., and Miyauchi, T., 2004, *J. Turbulence*, Vol. 5, pn. 16.

Peters, N., 1999, *J. Fluid Mech.*, Vol. 384, pp. 107-132.

Peters, N., 2000, London: Cambridge Press.

Poinsot, T. J., and Lele, S. K., 1992, *J. Comput. Phys.*, Vol. 101, pp. 104-129.

Poinsot, T. J., Echekki, T., and Mungal, M. G., 1992, *Combust. Sci. Technol.*, Vol. 81, pp. 45-73.

Pope, S. B., 1988, *Int. J. Eng. Sci.*, Vol. 26, pp. 445-469.

Prasad, A. K., 2000, *Expe. Fluids*, Vol. 29, pp. 103-116.

Seitzman, J. M., Haumann, J., and Hanson, R. K., 1987, *Appl. Opt.*, Vol. 26, pp. 2892-2899.

Seitzman, J. M., Miller, M. F., Island, T. C., and Hanson, R. K., 1994, *Proc. Combust. Inst.*, Vol. 25, pp. 1743-1750.

Sinibaldi, J. O., Driscoll, J. F., Mueller, C. J., Donber, J. M., and Carter, C. D., 2003, *Combust. Flame*, Vol. 133, pp. 323-334.

Smooke, M. D., Xu, Y., Zurn, R. M., Lin, P., Frank, J. H., and Long, M. B., 1992, *Proc. Combust. Inst.*, Vol. 24, pp. 813-821.

Sreedhara, S., and Lakshmisha, K. N., 2002, *Proc. Combust. Inst.*, Vol. 29, pp. 2051-2059.

Tanahashi, M., Miyauchi, T., and Ikeda, J., 1997, *Proc. 11th Symp. Turbulent Shear Flows*, Vol. 1, pp. 4-17.

Tanahashi, M., Fujimura, M., and Miyauchi, T., 2000a, *Proc. Combust. Inst.*, Vol. 28, pp. 529-535.

Tanahashi, M., Iwase, S., Uddin, A., Takada, N., and Miyauchi, T., 2000b, *Therm. Sci. Eng.*, Vol. 8, pp. 29-38.

Tanahashi, M., Iwase, S., and Miyauchi, T., 2001, *J. Turbulence*, pp. 2-6.

Tanahashi, M., Nada, Y., Ito, Y., and Miyauchi, T., 2002, *Proc. Combust. Inst.*, Vol. 29, pp. 2041-2049.

Tanahashi, M., Kang, S.-J., Miyamoto, T., Shiokawa, S., and Miyauchi, T., 2004a, *Int. J. Heat Fluid Flow*, Vol. 25 pp. 331-340.

Tanahashi, M., Nada, Y., and Miyauchi, T., 2004b, *Proc. 6th World Congr. Comput. Mech.*, CD-ROM (181).

Tanahashi, M., Kikuta, S., Nada, Y., Shiwaku, N., and Miyauchi, T., 2005a, *Proc. 4th Int. Symp. Turbulence and Shear Flow Phenomena*, Vol. 2, pp. 775-780.

Tanahashi, M., Murakami, S., Choi, G.-M., Fukuchi, Y., and Miyauchi, T., 2005b, *Proc. Combust. Inst.*, Vol. 30, pp. 1665-1672.

Tanahashi, M., Taka, S., and Miyauchi, T., 2006a, *Exp. Fluids*, Submitted.

Tanahashi, M., Inoue, S., Shimura, M., Taka, S., Choi, G.-M., and Miyauchi, T., 2006b, *Exp. Fluids*, Submitted.

Terakado, K., Matsuura, S., Choi, G.-M., Tanahashi, M., and Miyauchi, T., 2007, *Proc. 2007 ASME-JSME Therm. Eng. Summer Heat Transfer Conf.*, HT2007-37748.

van Oijen, J. A., Groot, G. R. A., Bastiaans, R. J. M., and de Goey, L. P. H., 2005, *Proc. Combust. Inst.*, Vol. 30, pp. 657-664.

Watson, K. A., Lyons, K. M., Carter, C. D., and Donbar, J. M., 2002, *Proc. Combust. Inst.*, Vol. 29, pp. 1905-1912.

Williams, F. A., 1985, California: Benjamin Cummings.

Williams, F. A., 2000, *Prog. Energy Combust. Sci.*, Vol. 26, pp. 657-682.